Experimental analysis of droplet spatial distribution in a spray burner

Olivier Rouzaud, Maxime Vicentini, Renaud Lecourt, Olivier Simonin, Virginel Bodoc, Pascal Fede

EXPERIMENTAL ANALYSIS OF DROPLET SPATIAL DISTRIBUTION IN A SPRAY BURNER

O. Rouzaud,[1,] M. Vicentini,[2] R. Lecourt,[3] O. Simonin,[4] V. Bodoc,[1] & P. Fede[4]*

[1]*Multiphysics for Energetics Dept., ONERA, Toulouse, France*
[2]*CNES, Paris, France*
[3]*Multiphysics for Energetics Dept., ONERA, Fauga-Mauzac, France*
[4]*Institut de Mécanique des Fluides de Toulouse (IMFT), Université de Toulouse, CNRS, Toulouse, France*

*Address all correspondence to: O. Rouzaud, Multiphysics for Energetics Dept., ONERA, Toulouse, France, E-mail: rouzaud@onera.fr

A new experimental setup PROMETHEE has been built to study spray combustion. The design corresponds to a square-duct channel with a bluff body spanning over the entire width of the channel. Turbulent flow circulates around the obstacle and liquid fuel is injected at the rear of the body through a flat-fan nozzle. The two-dimensional configuration has been chosen to facilitate the optical measurements, and the operating conditions partially reproduce those encountered inside a turboreactor. A procedure based on Mie scattering images is proposed to characterize the interdroplet distance to the nearest neighbor and to describe the spray spatial distribution. Such a procedure could benefit spray combustion modeling, providing a more precise length scale. First, the droplet spatial distribution under reacting conditions was investigated with respect to the interdroplet distance and the spatial distribution law at six locations downstream from the bluff body for the PROMETHEE experiments. For the distribution law, comparisons between the experimental, theoretical uniform, and uniformly random distributions, and numerical results from an in-house Monte-Carlo solver show that the distribution is close to the uniformly random one and that the interdroplet distance and its standard deviation evolve linearly with respect to the inverse of the density number square root. In addition, the numerical approach was used to estimate the projection and restriction errors associated with the interdroplet distance. Second, the procedure has been assessed through six Direct Numerical Simulation—Direct Particle Simulation (DNS/DPS) isotropic homogeneous turbulent simulations to highlight the clustering effects on the dimensionless mean and standard deviation of the nearest-neighbor interdroplet distance when decreasing the Stokes number. The results show that the droplet distribution is similar to the uniformly random distribution when the particle Stokes number is high enough while the mean (standard deviation) decreases (increases) with the reduction of the Stokes number due to the clustering effect. Such an observation demonstrates that preferential segregation is probably not important in the present experimental data.

KEY WORDS: *two-phase flow, spray spatial distribution, interdroplet distance*

1. INTRODUCTION

Gaseous combustion inside a combustion chamber has been studied for a long time due to its importance in industrial applications. However, spray combustion necessitates specific attention because injecting a liquid fuel inside a combustion chamber involves many different phenomena, like liquid atomization, evaporation, and the formation of a film on the chamber walls, which are not present in the purely gaseous case. Among the different questions, a point of interest is the determination of the global burning of a spray and the possible collective effects between the droplets. In both theoretical and numerical approaches as presented in the next paragraph, it is usually addressed by considering that a representative length scale of the droplet interdistance is equal to the mean droplet density at one-third power. While such an estimate is always valuable to build models, for instance, a more precise value of this scale—and the associated nearest-neighbor interdroplet distance distribution and spray spatial distribution—could be beneficial for modeling spray evaporation and combustion.

Starting from the works of Godsave (1953) or Spalding (1953) on the combustion of an isolated droplet of fuel, efforts have been made in the past on the theoretical, numerical, or experimental grounds to answer this question (Annamalai and Ryan, 1992). In the 1980s, various research groups developed theoretical models describing spray combustion (Chiu et al., 1982; Correa and Sichel, 1982; Kerstein and Law, 1982). For instance, Chiu and his coworkers proposed the concept of droplet group combustion, considering a droplet cloud with monodisperse droplets arrayed at uniform intervals. The distance is deduced from the average density number of the cloud $\bar{n}$. They proposed a droplet group combustion diagram with four spray combustion regimes: single droplet combustion, internal group combustion, external group combustion, and external sheath combustion [see Fig. 1 of Chiu et al. (1982)]. The regimes were classified through a group combustion number G (Jiang and Chiu, 1987):

$$G = 1.5\,\mathrm{Le}\left(1 + 0.276\,\mathrm{Sc}^{1/3}\,\mathrm{Re}^{1/2}\right)N^{2/3}\frac{d}{D_i} \tag{1}$$

where Le is the Lewis number, Sc is the Schmidt number, Re is the Reynolds number based on the droplet slip velocity, N is the total number of droplets contained in the cluster, d is the droplet diameter, and D_i is the mean distance between droplet centers. Since then, various group combustion diagrams have been proposed (Borghi and Champion, 2020; Candel et al., 1999; Reveillon and Vervisch, 2005). Borghi proposed a description of spray combustion in a premixed flow based on the Kerstein and Law model. The value $n^{1/3}r_F$, a ratio between the flame radius r_F around a single droplet and the uniform distance given by the droplet density number n, depends on the ratio d/e_L, where e_L represents the flame thickness. For values $n^{1/3}r_F < 0.41$, droplets burn in groups. For values $n^{1/3}r_F > 0.73$, pockets of gas are surrounded by flames. The intermediate case is a combination of the first two, in addition to the presence of a diffusion flame. Reveillon and Vervisch based their combustion diagram on some numerical simulations of a turbulent dilute-spray jet flame. Direct numerical simulation was used for the gaseous phase and a Lagrangian description was used for the spray. Particular attention was paid to the influence of the equivalence ratio and the dilute-spray density. Concerning the theoretical/analytical models, refer to the review paper by Annamalai and Ryan (1992), which describes several interaction models, from two droplets to arrays of droplets, and involves many different methods. One of the most interesting approaches is that proposed by Elperin and Krasovitov (1994). They considered a random cluster of polydisperse droplets in evaporation or combustion, using an irreducible multipole method. However, analytical models such as the previous one usually rest

on some simplifying assumptions, like a uniform distance between droplets, gas at rest, or the constancy of the Lewis number $\mathrm{Le} = 1$, which are hardly ever encountered in real situations.

On the numerical side, spray combustion in most industrial solvers is generally based on the isolated droplet model under evaporation using the point-source approximation. Although some works have been done to describe the behavior of an isolated droplet in combustion more precisely (Beck et al., 2008, 2009) or to provide results regarding the influence of droplet density on vaporization and combustion in the case of droplet arrays (Imaoka and Sirignano, 2005a,b), we discuss only spray models. Chiu and some of his coworkers (Jiang and Chiu, 1987, 1997, 2002) proposed several different approaches. In the most complex case (Jiang and Chiu, 1997), the modeling refers to a droplet multistate behavior accounting for its ignition, the presence of a wake flame or an envelope flame, and the flame extinction. The droplet state is chosen by comparing several specific Damkholer numbers and the local Damkholer number. The ignition and extinction numbers are based on the asymptotic theory set forth by Law (1975) and Mawid and Aggarwal (1989). As pointed out by Law and Chung (1980), improvement of the droplet ignition criterion would necessitate defining a characteristic length representative of the droplet distance. On their part, Wang and his colleagues (Wang et al., 2013) proposed to extend the evaporation model by considering four criteria: comparison of the evaporation and ignition delay time scales, respect of the flammability limit by the local fuel–air ratio, a minimal local temperature value, and a minimal droplet diameter value. The values of the last two criteria are respectively fixed at 1200 K and 1 micrometer. Assessment of the model is based on a large eddy simulation of an annular configuration with flow air for a methanol air spray flame. Finally, Paulhiac (2015) and Paulhiac et al. (2020) also proposed a multistate model, called Mustard, for spray combustion. Compared to the previous model, Paulhiac introduces an ignition time delay and considers only an envelope flame for a burning droplet. In addition, the first step of the model determines the possible state of the droplet; that is, the vaporization state or envelope flame state. In order to do so, the interdroplet distance is estimated from the local liquid volume fraction or, equivalently, the mean local droplet density n. Such a model has been applied to large real-scale simulations.

On the experimental side, McDonnell et al. (1992) examined the structures of methanol sprays obtained by air-assisted or pressure-swirl atomizers under nonreacting and reacting conditions. Two-phase flow characterization is based on phase Doppler anemometry (PDA) and the infrared extinction/scattering method. In the case of swirling air-assisted spray, the analysis focuses on the differences between gas velocities, droplet velocities and diameters, and vapor concentration for both kinds of conditions. On their part, Akamatsu et al. (1996) and Hwang et al. (2007) worked on a premixed kerosene spray flowing through an annular burner. They performed simultaneous measurements of OH- and CH-light emissions, droplet Mie scattering emission, and droplet size and velocity using PDA. From their experimental data, Akamatsu and coworkers concluded that droplet clusters are present, but the local aspect of some measurements makes this issue questionable with regard to its extent or its presence. The authors also note that for many clusters, the group combustion mode does not correspond to Chiu's classification. Indeed, some assumptions are not supported by the experimental spray, such as the sphericity of the cluster or the flow uniformity.

More recently, Beck et al. (2008, 2009) studied the effect of incomplete droplet prevaporization on NOx emissions in lean direct injection systems. In this experiment, two liquid fuel injectors are used to control the degree of prevaporization. The first one is far upstream of the combustion chamber and generates a fully prevaporized premixed incoming mixture. The second injector is located at the combustor inlet inside a swirl system, enabling the aerodynamic stabilization of the flame. Spray characterization has been performed using PDA and simultaneous

CH-planar fluorescence imaging (PLIF)/Mie scattering. Isolated droplets burn in the very dilute part of the flow under two possible regimes: an envelope flame surrounding the droplet or a wake flame behind the droplet. According to their numerical analysis, these regimes have a significant influence on NOx emissions.

Two-phase flow combustion has also been studied by Lovett et al. (2014), within the framework of bluff body stabilized flames for a non-premixed, jet-in-crossflow fuel injection. Results on the flame structure are discussed in relation to classical combustion reaction zone regimes. Experimental analysis is mainly based on chemiluminescence and PLIF of OH radicals, to understand the development of the reactive zones with respect to the fuel injection or the upstream flow conditions. In all of these works, the characterization of the droplet spray in terms of spatial distribution or interdroplet distance is not addressed.

Finally, the work of Sahu, Hardalupas, and Taylor (Sahu et al., 2014, 2016, 2018) provides one of the most comprehensive descriptions of the interaction between a spray and a turbulent flow. The experimental apparatus consists of a vertical test rig. Water or acetone is injected through an air-assisted nozzle inside a quiescent air flow characterized by large r m.s. velocities at ambient pressure and temperature. Nonevaporative water spray is used as a point of comparison with the evaporating acetone spray. Simultaneous coupling between interferometric laser imaging for droplet sizing (ILIDS) and PLIF measurements can describe the behavior of the spray. Thorough analysis is based on some correlations like the one between the fluctuations of droplet number densities and vapor mass fractions. Sahu and his colleagues also investigated the occurence of clusters of droplets and described their presence with respect to Chiu's theory thanks to a group evaporation number G. Such an approach should be extended to more realistic configurations with a swirling flow and under reacting conditions.

This short review of the experimental studies shows that, although various aspects of spray combustion have been—and are still being—addressed, constituting an exhaustive experimental database could be of primary importance for increasing our knowledge of such flows and for assessing numerical approaches. Thus a new experimental device, the Prométhée-LACOM test rig, has been developed to study reacting and nonreacting two-phase flow (Rouzaud et al., 2016; Vicentini et al., 2014, 2015). The configuration corresponds to a turbulent air flow circulating around a bluff body in a square-section channel. Liquid fuel is injected at the rear face of the bluff body through a flat-fan atomizer. The obstacle also acts as a flameholder. The setup has been designed to facilitate experimental observations and to reproduce, at least partially, the operating conditions of an aero-engine combustion chamber. The former constraint has been achieved by retaining a two-dimensional geometrical configuration. Characterization of the nonreacting flow has been presented elsewhere (Vicentini et al., 2014) and the scope of the paper is thus limited to the reacting case. More particularly, emphasis is laid on the droplet spatial distribution; that is, the interdroplet spacing and spatial distribution law. To the best of our knowledge, such a characterization has not been done for burning sprays, but realized in other fields like metallography (Bansal and Ardell, 1972), particle transport (Neumann and Umhauer, 1991) and meteorology (Kostinski and Jameson, 2000; Kostinski and Shaw, 2001). A usual analysis considers the clustering of the particles with several available treatments like the Cluster Index (Monchaux et al., 2012). For instance, Kostinski et al. demonstrated that the spatial distribution of particles inside a cloud is described rather by a Poisson mixture process than by a Poisson process (uniformly random distribution; Chandrasekhar, 1943). In our case, the spray analysis is based on a straightforward analysis of droplet Mie scattering data.

After a description of the experimental apparatus and operating conditions in Section 4, the methodology employed to process the droplet Mie scattering data is presented in Section 3. Such

a procedure was used to estimate, as locally as possible, values of the spray density number and of the average nearest-neighbor interdroplet distance in the flow based on images. Since the analysis of the experimental data has also been extended to the spatial distribution law, this section also contains a short reminder of two theoretical spray distributions, the uniform and uniformly random distributions, which will be used for comparison with our data, and a description of an in-house Monte-Carlo solver developed to further support the analysis. This reproduces a spray with uniformly randomly distributed droplets. Results are presented in Section 4. At first, the method was used with the experimental droplet Mie scattering data. Six different locations in the flow were chosen in order to describe the spray evolution inside the channel. It constitutes the main objective of this paper and brings answers to the question addressed at the end of the first paragraph, the description of a nearest-neighbor interdroplet distance and spray spatial distributions. The method was also applied to Direct Numerical Simulation—Direct Particle Simulation (DNS/DPS) with an isotropic homogeneous turbulence field. Six different cases were considered with different Stokes particle numbers to assess the interest of the present procedure and tentatively the influence of the clustering effect on the analysis.

2. EXPERIMENTAL SETUP AND MEASUREMENTS

2.1 Test Setup

A new air-breathing propulsion test setup, Prométhée-LACOM, has been recently developed at ONERA (see Fig. 1) to study spray combustion. The air feeding system is made up of a large pressure vessel, gas pressure regulators, and an electric heater (1 MW). The air mass flow rate is measured with a sonic nozzle located downstream of the electric heater ($\pm$ 3.3% accuracy). Subsequently, the preheated air stream passes through a succession of flow conditioners and turbulence grid. The test chamber consists of a square internal section (120 mm $\times$ 120 mm). The confined turbulent air stream flows around a fuel injection system prior to the combustion chamber. The injection system consists of a bluff body in which a liquid fuel nozzle is mounted. The bluff body spans over the entire width of the test section. The fuel feeding line is equipped with a Coriolis flowmeter ($\pm$ 0.2% accuracy). The spray nozzle is centered and screwed into the rear face of the obstacle. A spray of droplets is generated downstream directly into the combustion chamber. The fuel injector corresponds to a flat fan nozzle that produces an elliptical-shaped polydisperse spray. The spray opening angles of the major and minor axis are respectively 150° and 25°. The wide angle is set up to spray toward the upper and lower walls of the combustor. Note that in this study, the injector provides a nonsymmetrical spray with a larger number of droplets in the lower part of the flow. Such a feature let us consider different droplet density numbers in the upper and lower parts of the flow. The water-cooled combustor is equipped with three UV-transparent windows that can perform optical measurements downstream of the injection system. Ignition of the air–fuel mixture is triggered by a hydrogen-oxygen torch. The burnt gases are ejected into the exhaust pipe. This setup partially reproduces the main features of the

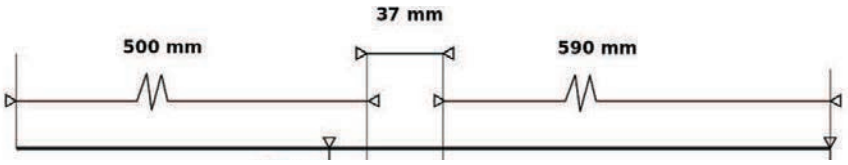

FIG. 1: View of the test setup

flow inside an actual aero-engine combustor. The air flow is confined, turbulent, and exhibits instabilities and large-scale structures. Besides, the flame is anchored aerodynamically by creating a main recirculation zone. The fuel–air equivalence ratio replicates the operating lean-burn conditions during a flight phase at cruising speed. A previous sizing study has been carried out on a prototype in 1:1 scale to choose the bluff body geometry (Vicentini et al., 2014) under nonreacting conditions. For a 6 m/s inert bulk airflow velocity at 298 K, a vortex-shedding phenomenon and a large recirculation zone are observed downstream of the bluff body. The criterion of choice for the bluff body geometry and dimensions was based on the intensity of the pressure signal measured on the bluff body upper and lower faces with respect to the noise. As a result, a trapezoidal bluff body with a 42% ratio blockage, defined as the ratio of the projected area of the obstacle upon the unobstructed cross section of the channel, has been retained (Fig. 1). Note that in reacting conditions, the von Kármán vortex street is no longer observed while the recirculation zone is still present. A large number of droplets is expected to be located around the vertical mid-plane of the combustor. Since some of the experimental diagnostics used are planar (imaging devices), the configuration promotes the measurement of many relevant flow data (droplets positions, sizes, velocities, and flame position) compared to an axisymmetric one.

The n-decane is selected as a surrogate fuel because it has chemical properties close to kerosene ones (density, surface tension, auto-ignition temperature). Furthermore, evaporation or chemical kinetics modeling are much simpler for a monocomponent fuel than for a mixture, should this configuration be calculated. Under nonreactive conditions, the droplet spray is polydisperse with droplet sizes from 10 to 150 µm (Vicentini et al., 2014).

2.2 Operating Conditions

Although nonreacting and reacting two-phase flows have been investigated, we only consider reacting flow in this paper. The nominal operating point is set at an air mass flow rate equal to 64 g/s. At the combustor inlet, the air flow is at standard atmospheric pressure and 450 K. The corrected mass flow rate corresponds to 1.36 kg/s/bar/K$^{1/2}$. Since the combustion section is 120 mm $\times$ 120 mm, the bulk airflow velocity is close to 6 m/s. Consequently, the Reynolds number based on the hydraulic diameter is about 22,000. The liquid fuel temperature is measured just upstream from the nozzle and is equal to 330 K. The n-decane fuel (95% purity) is injected at 1 g/s to provide 44 kW thermal power. Therefore the fuel–air equivalence ratio is around 0.24. The water cooling of the combustion chamber protects the inner walls ($T_{\mathrm{wall}} < 650$ K) and we can perform tests lasting several tens of minutes.

2.3 Implementation of Measurements

The main objective of the experimental program is to build a spray combustion database for a better understanding of droplet combustion and for the assessment of numerical approaches. In order to do so, gaseous and liquid phases have been studied in nonreacting and reacting conditions. Concerning the reacting conditions, we employ OH-PLIF imaging, droplet Mie imaging, and phase Doppler interferometry (PDI) techniques. Chemiluminescence and OH-PLIF imaging are employed to study the hot regions of the flow. The first technique uses spontaneous emission of the OH flame marker while in the second technique, excitation of the marker is produced using of a laser. Droplets illuminated by a laser sheet generate light through the Mie scaterring process. The light is captured by a camera in order to evaluate the positions of droplets. Simultaneous OH-PLIF and Mie scaterring measurements provide instantaneous information about

the droplet spatial distribution with respect to the reacting zones. Finally, application of a two-component PDI measures the instantaneous droplet velocities (longitudinal, transverse) and their sizes. Except for the OH-chimiluminescence, all the measurements have been performed in the vertical mid-plane of the combustor.

Figure 2 presents the optical system for both OH-PLIF and Mie scattering techniques. Due to the scope of the paper, we only give details on the Mie scattering setup. To light droplets, a millimetric thin laser sheet is produced with a high-frequency Nd:YLF laser Quantronix Darwin ($\lambda = 527$ nm) using a cylindrical lens. The laser sheet crosses the combustion chamber from the bottom window. The frequency of the system is fixed to 1 kHz with a laser pulse duration around 200 ns. A high-speed camera Phantom V341 is positioned aside to capture the Mie scatterred light from the droplets through a lateral window of the combustor. Image resolution is 1792 pixels $\times$ 1600 pixels. In the sequel, analysis of Mie scaterring is performed in six specific regions of the flow, considering only small parts of the overall Mie image (Table 1). Such a choice allows a relatively local characterization of the spray. Figure 3 presents a typical superimposition of the PLIF-OH and Mie scaterring images at the same time in the upper part of the wind tunnel behind the obstacle. The origin point of the frame of reference is located on the lower wall of

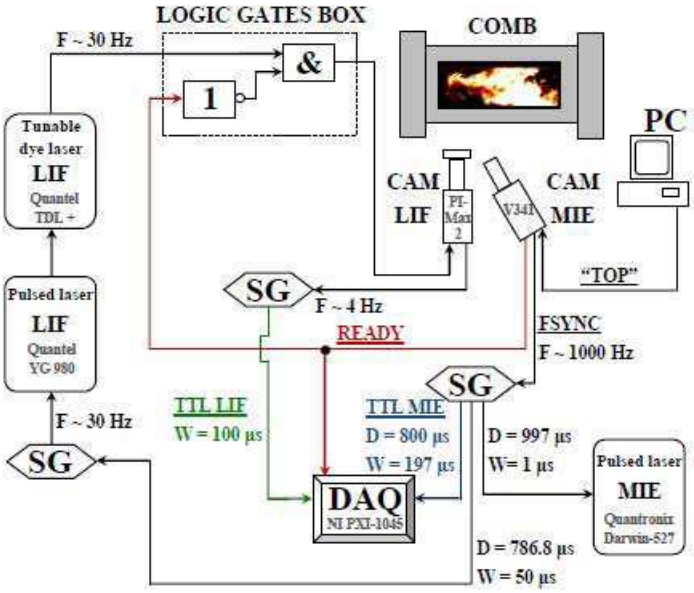

FIG. 2: Setting and digital timing diagram for the synchronization of OH-PLIF and Mie scattering imaging

TABLE 1: Centers and sizes of the analysis windows

Window	Coordinates (mm)	Window size (μm^2)
I	(17, 52)	993 $\times$ 993
II	(31, 63)	3319 $\times$ 3319
III	(49, 76)	5673 $\times$ 5673
IV	(19, 39)	2837 $\times$ 2837
V	(31, 41)	1986 $\times$ 1986
VI	(49, 28)	5673 $\times$ 5673

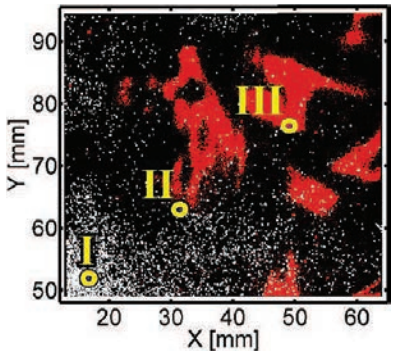

FIG. 3: Simultaneous PLIF-OH and Mie images

the channel and aligned with the rear part of the obstacle. The injection axis is at 60 millimeters above it. The red or light zones correspond to the hot regions detected by the PLIF-OH system. The droplets are in white and their sizes have been enlarged to make them visible on the image. The significance of the Roman numbers will be explained later.

3. SPRAY ANALYSIS

3.1 Analysis of the Interdroplet Distance

Since the experimental work is based on Mie scattering images, we have at our disposal a certain number N^{Mie} of them. Several steps are needed before performing a statistical analysis on the interdroplet distance D_i. As a preliminary remark, we have to mention that the droplets are located in a volume of which the dimensions correspond to the size of the Mie scattering image times the thickness of the laser sheet ϵ (close to 1 millimeter in this case). It means that the interdroplet distance is based on the orthogonal projection of the droplets from the measurement volume to the image surface (projection process, Fig. 4).

At first, each image R has been processed to suppress the soot luminance and the particles that are out of the depth of field. To meet the first objective, a smoothing method, based on a sliding-window algorithm (16 pixels $\times$ 16 pixels), is applied. This algorithm acts as a linear low-pass filter on the luminance intensity. Concerning the out-of-depth of field particles, we define a threshold value for the light intensity (value of 85 out of 4095 levels) and retain only the droplets with scattered-light intensity above this level.

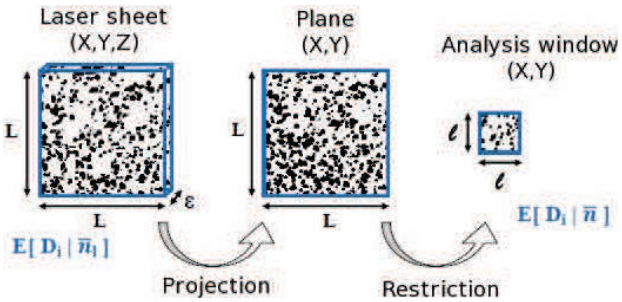

FIG. 4: Description of the data processing for the error analysis

The second step consists of determining the mean density number of particles $\bar{n}$ over all the images. By denoting N^R the number of particles in the current image R, the associated density number per unit surface n^R is straightforwardly given by

$$n^R = \frac{N^R}{\text{Window area}} \tag{2}$$

leading to the definition of the mean density number

$$\bar{n} = \frac{1}{N^{\text{Mie}}} \sum_{R=1}^{N^{\text{Mie}}} n^R \tag{3}$$

Determination of the interdroplet distance constitutes the next step of the data processing. For each droplet S in an image R, its center of gravity is deduced from the first-order moment integral of its pixel coordinates according to

$$\begin{cases} X^{R,S} = \dfrac{1}{\mathcal{A}^S} \displaystyle\int\int_{\mathcal{A}} X \, dX dY \\ Y^{R,S} = \dfrac{1}{\mathcal{A}^S} \displaystyle\int\int_{\mathcal{A}} Y \, dX dY \end{cases} \tag{4}$$

where $\mathcal{A}^S$ is the droplet area. The interdroplet distance $D_i^{R,S}$ is the minimal value of the Euclidean distance between the Sth droplet and all other droplets $S*$ belonging to the same image,

$$D_i^{R,S} = \underset{\forall S* \neq S}{\text{Min}} \left[\sqrt{(X^{R,S} - X^{R,S*})^2 + (Y^{R,S} - Y^{R,S*})^2} \right] \tag{5}$$

Once all the images have been processed, the mean value and the standard deviation of the interdroplet distance are evaluated as

$$\mathsf{E}\left[D_i\right] = \frac{1}{N^{\text{Mie}} N^R} \sum_{R=1}^{N^{\text{Mie}}} \sum_{S=1}^{N^R} D_i^{R,S} \tag{6}$$

and

$$\mathsf{SD}\left[D_i\right] = \sqrt{\frac{1}{N^{\text{Mie}} N^R} \sum_{R=1}^{N^{\text{Mie}}} \sum_{S=1}^{N^R} \left(D_i^{R,S} - \mathsf{E}\left[D_i\right] \right)^2} \tag{7}$$

An additional quantity is the equivalent regular distance D_i^{unif} written as

$$D_i^{\text{unif}} = \frac{1}{N^{\text{Mie}}} \sum_{R=1}^{N^{\text{Mie}}} \left[n^R \right]^{-1/2} \tag{8}$$

Such a distance is often used to underline the neighborhood effects between droplets in evaporation or in combustion ratio, through the distance parameter C, between this distance and the droplet diameter or the flame diameter around a droplet. For instance, according to Crowe et al. (2011) and Virepinte et al. (1999), there is no interaction between two droplets in terms of evaporation for a distance parameter from 10 to 15. Simulations of Imaoka and Sirignano (2005a,b)

on droplet arrays confirm that the evaporation/combustion interaction is quite reduced over a certain value of the distance parameter. In most aeronautical combustion chambers, the value of this parameter is between 5 and 40 (Candel et al., 1999; Correa and Sichel, 1982).

At this point, the experimental procedure to get the quantities of interest from the Mie scattering images has been established. However, two additional remarks have to be made to fully describe the experimental results that will be presented in the next section. First, only restricted parts of the images, the so-called analysis windows in the sequel, are taken into account during the restriction process (Fig. 4). These windows are square-shaped with an edge length l. The reason for such a choice is that, since the spray is not at all uniformly distributed inside the test section, averaging over all the droplets of all the images will produce quite inaccurate values of interest. On the contrary, by carefully choosing the sizes of the analysis windows, we may expect to get local values of the quantities of interest with a sufficient number of droplets to perform a relevant statistical analysis on these values. In this analysis, six analysis windows have been located in different parts of the Mie scattering images in order to describe the spatial evolution of the spray. Their locations have been chosen empirically using the Mie images to describe different positions in the two-phase flow and different mean density numbers. Their sizes vary from 35×35 to 200×200 pixels depending on their locations inside the flow.

Second, the values provided by Eq. (5) may be biased by at least two sources of errors (Fig. 4). The first one, called the projection error, is due to the orthogonal projection of the droplets from the probe volume to the image surface previously mentioned. Most of the time, it leads to an underestimation of the distance between two droplets when they are not in a plane perpendicular to the projection direction. Occasionally, the distance is conserved when the two droplets are inside a plane perpendicular to the projection direction. The second type of error comes from the restriction process, described below and illustrated in Fig. 4. When considering a droplet inside an analysis window, it may happen that its nearest-neighbor droplet is not in the analysis window itself but just outside of it. In that case, the droplet distance is systematically overestimated and its associated error is called the restriction error or border zone effect as mentioned by Neumann and Umhauer (1991). A last comment arises about a third source of error associated with the presence of preferential segregation in the spray. This question will be partially addressed in Section 4.2.

Finally, although this procedure has been developed primarily for Mie scattering images, its extension to a three-dimensional field of droplets, like the ones obtained by a two-phase flow simulation, is quite straightforward. We have to replace the window area and the density number per unit surface in Eqs. (2) and (3) by a window volume and mean density number per unit volume

$$n_{3D}^{R} = \frac{N^{R}}{\text{Window volume}} \tag{9}$$

$$\bar{n}_{3D} = \frac{1}{N^{\text{Mie}}} \sum_{R=1}^{N^{\text{Mie}}} n_{3D}^{R} \tag{10}$$

An additional feature is to account for the third coordinate of the barycenter droplet $Z^{R,S}$ and the distance between a pair of droplets:

$$D_i^{R,S} = \underset{\forall S* \neq S}{\text{Min}} \left[\sqrt{(X^{R,S} - X^{R,S*})^2 + (Y^{R,S} - Y^{R,S*})^2 + (Z^{R,S} - Z^{R,S*})^2} \right] \tag{11}$$

In the next section, such a procedure will be applied to a DNS/DPS simulation to extract data on

the droplet spatial distribution, starting from the second step of the procedure, thus avoiding the projection step.

3.2 Analysis of the Spray Spatial Distribution

To get further insight in the spray organization, we can also try to characterize the spatial distribution of the droplets in each analysis window by comparison with the uniform (droplets arrayed at uniform intervals) and the uniformly random distributions. In the two-dimensional case, given a mean surfacic density number $\bar{n}$, the interdroplet distance between nearest neighbor writes, in the case of the uniform distribution, as

$$D_i^{\mathrm{unif}} = \bar{n}^{-1/2} \tag{12}$$

while in the three-dimensional case, we have

$$D_i^{\mathrm{unif}} = \bar{n}_{3D}^{-1/3} \tag{13}$$

where $\bar{n}_{3D}$ represents the usual mean density number. Note that the standard deviation is null for this type of distribution in all cases. The Hertz–Chandrasekhar distribution refers to a distribution where the droplets or the particles are uniformly randomly dispersed. Using the Hertz–Chandrasekhar theory (see Appendix), we can demonstrate that, in the two-dimensional case, the mean distance and its standard deviation are expressed as

$$\mathsf{E}\left[D_i^{H-C}\right] = 0.5\,\bar{n}^{-1/2}, \quad \mathsf{SD}\left[D_i^{H-C}\right] \approx 0.2613\,\bar{n}^{-1/2} \tag{14}$$

while the three-dimensional counterparts (Chandrasekhar, 1943) read as

$$\mathsf{E}\left[D_i^{H-C}\right] \approx 0.5539\,\bar{n}_{3D}^{-1/3}, \quad \mathsf{SD}\left[D_i^{H-C}\right] \approx 0.2013\,\bar{n}_{3D}^{-1/3} \tag{15}$$

Thus, for both laws, the interdroplet distance varies linearly with respect to either the inverse of the square-root of the surfacic density number $\bar{n}$ or the inverse of the cubic-root of the volumic density number $\bar{n}_{3D}$, but with different slope coefficients. In the sequel, we will compare the behavior of the experimental data with the two theoretical laws. Two main questions drive this comparison. The first one addresses the relevancy of the uniform distribution to describe a spray. Such a choice is often done to estimate the interdroplet distance and, possibly, used for modeling. The second one is to verify if a linear relationship between the interdroplet distance and the density number $\bar{n}$ exists in our experiment such as

$$\mathsf{E}\left[D_i\right] = \alpha\,\bar{n}^{-1/2} \tag{16}$$

and

$$\mathsf{SD}\left[D_i\right] = \beta\,\bar{n}^{-1/2} \tag{17}$$

Finally, to further support our analysis, we have developed a Monte-Carlo solver to compute the interdroplet distance for a set of point particles uniformly randomly dispersed. Although this configuration is not exactly similar to a real spray (the droplets are not pointwise), it is expected that such a solver will contribute to explain some of the tendancies of our results. The locations of the particles are randomly chosen into a three-dimensional volume of which the dimensions are provided by the user. The mean density number $\bar{n}_l$ is also specified but must be chosen according to the case under consideration. For instance, referring to the analysis of the Mie

scattering images, we can associate a surfacic mean density number $\bar{n}$ to an analysis window. To build a three-dimensional droplet distribution corresponding to $\bar{n}$, the mean number of particle per unit volume $\bar{n}_{3D}$ writes as

$$\bar{n}_{3D}\,\epsilon = \bar{n} \tag{18}$$

where ϵ represents the thickness of the three-dimensional slice. The previous relationship simply states that the number of particles is exactly the same in the three-dimensional volume and in the two-dimensional window. If the droplets are uniformly randomly dispersed, we can expect to approximate the three-dimensional field of droplets prior to the projection process, and to reproduce the projection and restriction steps of the experimental procedure.

4. RESULTS AND DISCUSSION

4.1 Spray Description

Figure 5 presents the system of coordinates and the locations of the analysis windows. The (X, Y) coordinates correspond respectively to the longitudinal and transversal axis, and are in the vertical mid-plane of the combustor. The origin of the frame of reference is on the lower wall of the channel. It is vertically aligned with the rear face of the bluff body. The center of the injection system is at coordinates $(0, 60)$ in millimeters. Downstream of the obstacle, we can see two OH-PLIF images taken in the upper part and in the lower part of the flow but not at the same instant. They have been assembled for a better understanding of the flow.

Figure 5 also indicates the position of the six windows of analysis that have been considered to study the droplet spatial distribution using Mie scattering images. The coordinates of the center of the six windows are given in Table 1. Two points are located in the upper part of the channel above $Y = 60$ mm and the others in the lower part. Their locations have been chosen in order to account for the spray density, the distance to the injection system, and the flame presence. The table also specifies the sizes of the analysis windows in micrometers. These sizes

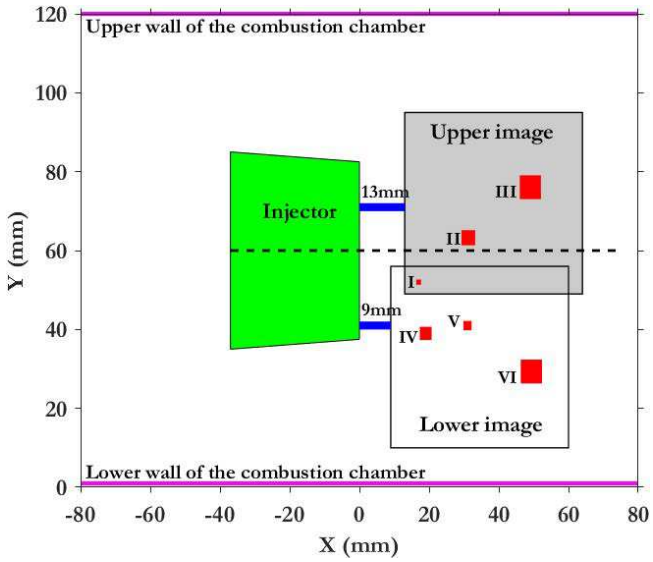

FIG. 5: Positions of the analysis window with respect to the obstacle

have been considered in order to provide statistical data on the spray distribution as locally and as accurately as possible. The local constraint means that the size of the window should not be too large to define values representative of the local spray distribution. On the accuracy part, a sufficient number of samples (droplet positions) is needed to perform reliable statistics. The next paragraph provides more details on this aspect.

The experimental work presented hereafter is split in two parts. The first part of the work deals with the experimental analysis of the center-to-center interdroplet distance to the nearest neighbor since this value is commonly considered in evaporating or reacting sprays to characterize droplet interactions. In the second part, the spray distribution law is investigated and compared to two existing laws, Hertz–Chandrasekhar and one meaning a cubic arrangement of droplets.

4.1.1 Droplet Spacing

4.1.1.1 Experimental Analysis of the Interdroplet Distance

For each analysis window, we have at our disposal $N^{\mathrm{Mie}} = 2000$ images. Table 2 summarizes the main results obtained at the six points under consideration. Starting from the second column, the data yield the number of samples, the mean density number $\bar{n}$, the mean interdroplet distance $\mathsf{E}[D_i]$ and its associated standard deviation $\mathsf{SD}[D_i]$, the so-called uniform distance D_i^{unif}, and the distance parameter $\bar{C}$. The last value corresponds to the ratio of the interdroplet distance to the local mean arithmetic droplet diameter d_{10}. This latter quantity is based on PDI measurements done inside each analysis window. The regular distance D_i^{unif} is calculated as if the droplets were uniformly arrayed inside the window.

A first comment bears on the evolution of the mean density number and the mean interdroplet distance. According to the data, the mean density number varies from a larger value close to the flat fan injection (point I) to smaller values far away (points III and VI). Such an evolution is consistent with the presence of the flame involving high-temperature and a more rapid evaporation of the smaller droplets compared to the nonreactive case (Vicentini, 2016). Indeed, there is a factor 20 in the density number at point III between the nonreacting and the reacting cases as observed by Vicentini. Note also that the quite dense spray at point I precludes the flame penetration close to the injection system as revealed by the Mie/OH-PLIF superimposed images (Vicentini, 2016). The mean interdroplet distance values are consistent with the mean density number behavior. In particular, it increases with the distance to the injection system. Referring to the distance parameter $\bar{C}$ in the last row, we note that the spray evolves between

TABLE 2: Outcomes of the experimental distributions of droplets

Window	**Nb. samples**	$\bar{n}$ **(1/cm^2)**	$E[D_i]$, $SD[D_i]$ **(µm, µm)**	D_i^{unif} **(µm)**	$\bar{C} = E[D_i]/d_{10}$
I	38 000	1 929	(178, 61)	228	4
II	56 100	258	(365, 217)	623	9
III	27 900	44	(860, 721)	1508	22
IV	33 900	215	(387, 245)	682	9
V	37 600	477	(248, 148)	458	7
VI	76 300	120	(503, 331)	913	12

droplet interactions and isolated droplet behaviors according to the admitted description (Crowe et al., 2011).

Second, we compare the interdroplet distance to the regular one. In all cases, the experimental values are smaller than the regular values derived from the experimental density number with a factor varying between 1.3 and 2. Thus, in this experiment, the regular distance is not the most representative distance for droplet interactions.

4.1.1.2 Size of the Analysis Windows

Since we intend to determine values of the droplet density number as local as possible, the size of the windows should be small with respect to the overall Mie image. On the other side, performing a statistical analysis on the interdroplet distance D_i requires considering a sufficient number of samples (droplets). Due to the spray inhomogeneity, the trade-off between these two constraints leads to choosing different sizes according to the window locations.

In the case of window I, Table 3 gathers the mean density number, the mean nearest-neighbor distance, and the associated standard deviation for three different sizes of the analysis window from simple to double. To choose the size of analysis window I, the main guidelines were to get a sufficient number of samples (arbitrarily fixed above 25,000) and to check that an increase or decrease of its size would provide limited differences as seen in Table 1. For the other analysis windows, the size of the analysis window has been approximately defined by the ratio of their density number to the density number of window I and we have checked that decreasing or increasing its size provided consistent results.

4.1.2 Droplet Spatial Distribution Law

To get further insight in the spray organization, we now try to characterize the spatial distribution of the droplets in each analysis window by comparison with droplets arrayed at uniform intervals and uniformly random distributions. Since the experimental values of the density number depend on Mie scattering images taken at different instants, we have decided to retain only the images of which the density number is close to the mean value $\bar{n}$ in order to limit the too-large density number fluctuations and to be as close as possible to the perfect conditions of the two theoretical laws. In this work, the selection criterion is fixed to $\pm$ 10%, meaning that we retain images for which $n \in [0.9\bar{n},\ 1.1\bar{n}]$. When compared to the results accounting for all the images, such a choice leads to a relative error on the mean interdroplet distance around 10% with a reduced standard deviation.

The mean distance and standard deviation of both theoretical and experimental distributions are plotted respectively in Fig. 6(left) and Fig. 6(right) for the six windows of analysis. The extremal values of the mean density number correspond to the windows for which the spray is respectively less or more dense. As mentioned in Section 2.1, the nonsymmetrical injection

TABLE 3: Influence of the size of an analysis window: window I

Window size (μm^2)	**Nb. samples**	$\bar{n}$ **(cm^2)**	$\mathsf{E}[D_i]$ **(µm)**	$\mathsf{SD}[D_i]$ **(µm)**
709×709	20,270	2016	183	64
993×993	38,000	1929	178	61
1390×1390	74,200	1920	171	58

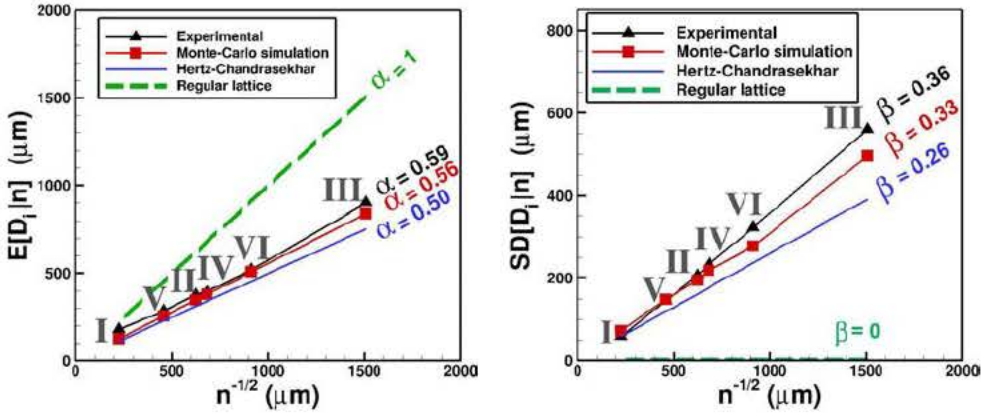

FIG. 6: Average interdroplet distance and standard deviation vs. the inverse square root of the density number

of the droplets leads to larger density numbers for windows I and V followed by window II. Window IV is located close to the spray edge while windows VI and III have the smallest density numbers due to their distance from the injector. At first, we will compare only the experimental distribution with the theoretical ones. It demonstrates that the experimental data are much closer to the Hertz–Chandrasekhar distribution than to the uniform one in each case. Furthermore, the evolution of the experimental mean distance can be approximated as a straight line according to

$$\mathrm{E}\,[D_i|\bar{n}] = \alpha\,\bar{n}^{-1/2} \tag{19}$$

with a value of the slope coefficient α equal to 0.59, a value to be compared to 0.5 for the uniformly random distribution and 1 for the uniform one. The same remark can be made for the standard deviation with a β-slope equal to 0.36 for the experimental data and equal to 0.26 for the Hertz–Chandrasekhar distribution. Note that the slope of the uniform distribution is null by definition.

Consider now the experimental processing of the Mie scattering images. It relies on a projection from a three-dimensional slab toward a two-dimensional image, followed by a restriction from a large image to a small image (Fig. 4). To further understand the experimental results, we have used the Monte-Carlo numerical tool previously described. A mean density number $\bar{n}$ is attached to each analysis window and, from these values, we can define an associated density number $\bar{n}_{3D}$ per unit volume according to Eq. (18). By using these density numbers, the Monte-Carlo approach lets us create an equivalent three-dimensional droplet field for each analysis window assuming the particles are randomly dispersed. From that point on, the process is completly equivalent to the experimental one. For each selected volume, the droplets are projected on a plane, the interdroplet nearest-neighbor distances are calculated, and statistical analysis is performed as previously. The associated results are presented on both images of Fig. 6 as random (simulation). They are in between the theoretical and the experimental curves but closer to the latter ones as confirmed by the slopes values. Such results seem to demonstrate that the three-dimensional experimental distribution is equivalent to the three-dimensional uniformly random distribution. The Monte-Carlo solver will now be used in the next paragraph to evaluate the error committed on the interdroplet distance.

4.1.3 Error Analysis

To estimate the accuracy of the experimental results on the droplet spacing or the spatial distribution, the evaluation of two different sources of error have been performed. The first one is associated with the identification of the droplet barycenters on each Mie scaterring image. The resolution of the images is 35.2 pixels per millimeter (one pixel corresponds to 28 micrometers). Thus the error committed on the barycenter coordinates of a spherical droplet is expected to be around 20 µm. Since the coordinates of two droplets are used to calculate their interdroplet distance, the error on this distance is, in the worst case, around 40 µm. Referring to Table 2, the relative error with respect to the mean distance $\mathsf{E}[D_i]$ varies between 4.5% and 22%.

Consider now the errors associated with the projection and restriction steps (Fig. 4). To assess their importance on the interdroplet distance, the Monte-Carlo numerical approach has been employed. Numerical droplets are randomly dispersed according to the Hertz–Chandrasekhar law inside a slab volume of which the dimensions are equivalent to the dimensions of the experimental Mie scattering images. The statistical analysis of the Monte-Carlo data follows the same procedure than the experimental one. The projection step consists of projecting the droplets on the (X, Y) plane, discarding the third coordinate. The interdroplet distance is then calculated for both three-dimensional and two-dimensional distributions, and the comparisons of these two values provide an estimation of the projection error.

In the next step—the restriction one—the large two-dimensional numerical image is split into a set of smaller images of which the sizes are comparable with the sizes of the analysis windows. Comparison of the interdroplet distance for the large image and the set of the smaller images provides an estimation of the restriction error. As previously mentioned, this difference is due to the fact that, for some droplets located in the border zone of a small image, its nearest-neighbor droplet is out of the image. Such a border zone effect (Neumann and Umhauer, 1991) is all the more important as the size of the image is smaller.

Table 4 summarizes the projection and restriction errors for the six analysis windows. The total error corresponds to their product. As expected, the projection step decreases the interdroplet distance (minus sign). The projection error is all the more important as the density number inside the measurement volume is large. Possible improvements would be to reduce the laser sheet thickness. On the other side, the restriction effect overestimates the interdroplet distance because of the border zone effect. Minimizing the error would be possible by adding an additional treatment for the droplets of which the distance to the image boundaries is smaller than its calculated interdroplet distance. In that case, we should either discard these droplets from the data or calculate their real interdroplet distance considering outer droplets.

Finally, we can also question the point particle approximation influence in the estimation of the nearest-neighbor distance. By point particle approximation, we mean that each particle is

TABLE 4: Estimation of the interdroplet distance errors

Window	Projection error	Restriction error	Total error estimation
I	–45%	+10%	–39%
II	–22%	+8%	–16%
III	–4%	+21%	+16%
IV	–20%	+11%	–12%
V	–31%	+10%	–23%
VI	–12%	+7%	–6%

described by the coordinates of its barycenter and that its size is not taken into account in the distance analysis. Bansal and Ardell (1972) have considered such an influence in three different cases: the nearest-neighbor spacing in a three-dimensional problem, the nearest-neighbor spacing of finite parallel cylinders in a two-dimensional problem, and the nearest-neighbor spacing in a plane section through a three-dimensional array of finite spheres. This last problem is very similar to our case. For volume fractions α_l lower than 0.01, Bansal and Ardell (1972) demonstrate that the point particle approximation provides very accurate results. Referring to the analysis windows, the largest value of the volume fraction is associated with window I and is equal to 0.005. Thus the point particle approximation yields consistent results.

4.2 Analysis of the Clustering Effect on Nearest-Neighbor Interdroplet Distance from DNS/DPS Simulations

For two-phase flows experiencing preferential segregation, the spray distribution will be modified compared to the uniformly random one. Therefore it is interesting to describe as far as possible the effect of some clustering effect on the values of the coefficients α and β. Such a description could also serve to complete the analysis of the present experimental data. In order to do so, numerical DNS/DPS have been used.

Fede et al. (2015) realized DNS/DPS calculations of solid particles. The particles are spherical and the spray is monodisperse with a particle diameter equal to 600 micrometers. The particles are submitted to an isotropic homogeneous turbulence inside a cubic box of 128 millimeters long containing 450,000 particles corresponding to a mean density number of $\bar{n} = 215$ per cubic centimeter. Six calculations have been done using six different particle densities and the Stokes number:

$$\mathrm{St} = \frac{\tau^F_{fp}}{\tau^t_{f@p}}$$

defined as the ratio of the fluid-particle relaxation time scale τ^F_{fp} to the turbulent Lagrangian time scale $\tau^t_{f@p}$, varies from 0.22 up to 4.58 (0.22, 0.43, 0.85, 1.70, 3.25, 4.58). Preferential concentration behavior is clearly exhibited for Stokes numbers lower than 1.70 as shown in Fede et al. (2015) (Fig. 13).

Previous methodology used for Mie scattering images processing has been applied to these fields, but in a three-dimensional configuration (see end of Section 3.1). More precisely, the computational domain has been cut in smaller cubic boxes with two different sampling lengths respectively equal to 30 and 45 millimeters. The average number of particles inside the smaller domains are respectively close to 6000 and 20,000. The numbers $\left(N^R, N^{\mathrm{Mie}}\right)$ are respectively equal to $(6000,\ 64)$ and $(20{,}000,\ 8)$ for the smallest length and the largest one. In a second step, droplet distances have been calculated and statistics performed to estimate the dimensionless mean and standard deviation α and β defined in Eqs. (16) and (17) but for a three-dimensional case. Their respective theoretical values according to the Hertz–Chandrasekhar theory are equal to 0.5539 and 0.2013. In that case, the projection error is null since we consider the real distance between droplets while the restriction error is still present.

The results are gathered in Fig. 7 presenting the α and β coefficients versus the Stokes number. At first, we note that, referring to the two plots, the α and β coefficients for the mean minimal distance and its standard deviation tend respectively to their theoretical values 0.5539 and 0.2013 with an increasing Stokes number. This tendancy is observed for both sizes of the sampling box. A second point of concern is the evolution of the α and β coefficients when the Stokes number

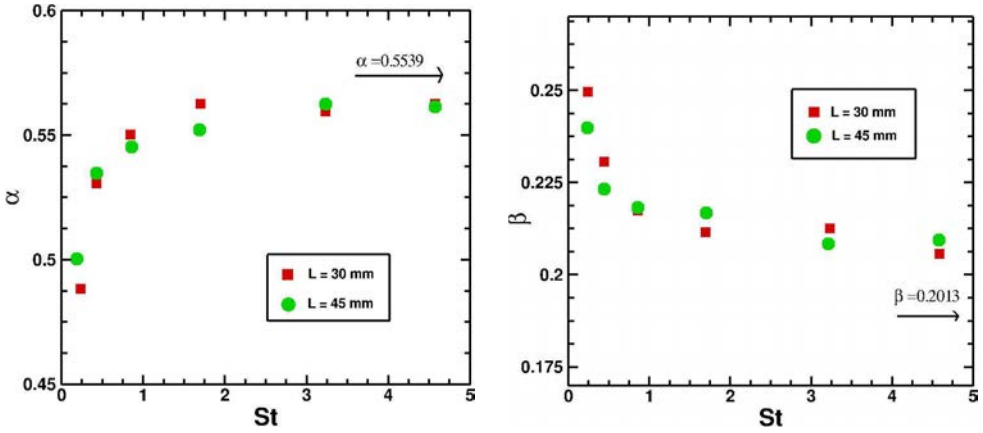

FIG. 7: Clustering effect

decreases, leading to a decrease of the interdroplet distance and an increase for the standard deviation. A possible explanation of this behavior is the enhancement of the segregation phenomenon, which becomes more and more important as the Stokes number decreases. This last effect is well known in the literature (Simonin et al., 2006; Squires and Eaton, 1991) although characterized differently. In a recent work, Boutsikakis (2020) performed several additional DNS simulations with a larger range of the Stokes number and observed the same tendencies on the coefficients evolutions. He also noticed that, below a certain value of the particle Stokes number, the α and β coefficients respectively increase and decrease, and seem to tend toward the values of an uniformly random distribution as the Stokes number tends to zero. However that may be, using the α and β coefficients seems appropriate to account for the clustering effect when considering a three-dimensional field of droplets. A last comment is about the sampling lengths, which provide similar results. Although no other sampling length has been tested, it is our belief that there is a range of sampling lengths that provide valuable results, while using too small or too large lengths may produce poor or inconsistent results (Monchaux et al., 2012).

Finally, if we refer to Fig. 6, we observe that the experimental data is above the Monte-Carlo simulation with the present procedure. Consider now two three-dimensional droplet fields with the same density number but associated respectively with a preferential segregation effect and the uniformly random distribution. Based on the analysis of the previous paragraph, the α coefficient of the first case with preferential segregation is lower than the α coefficient. Applying our experimental procedure to these two fields and assuming that the restriction errors is similar in both cases, the projection error will decrease their respective mean minimal distances. Thus we can expect that the mean minimal value as well as the α coefficient in the first case will still be lower than their counterparts in the uniformly random case. This is in contradiction with the plot of Fig. 6 and tend to prove that the clustering effect does not seem to play an important role in our experiment.

5. CONCLUSIONS

A new experimental setup (Prométhée-LACOM) has been designed to study spray combustion and provide an experimental database to acquire a better knowledge of such flows and for further assessment of the numerical approaches. The setup consists of a trapezoidal bluff body located

inside a square-channel duct. The upstream air flow is turbulent and liquid n-decane is injected at the rear face of the bluff body with a flat-fan atomizer. Operating conditions reproduce partially the conditions met inside an aero-engine combustor.

In this work, a method is proposed to estimate the interdroplet between nearest-neighbor particles from Mie scattering images and to characterize the spray spatial distribution, with a linear relationship between the square root of the mean density number and either the mean interdroplet distance or its standard deviation. The whole process has been applied to DNS/DPS simulations on one side, and to experimental data from Prométhée-LACOM setup on the other side.

Measurements have been done for both nonreacting and reacting cases to describe the gaseous and the liquid phases. In the paper, emphasis is laid on the spray distribution in the reacting case. At first, using droplet Mie scattering helped to estimate as local as possible values of the droplet density number in six regions of the flow and to derive values of the interdroplet distance between nearest-neighbor particles. This distance is believed to be an important parameter since it is often used to characterize droplet interactions by comparison with the droplet diameter or the droplet flame diameter. Further data analysis using Monte-Carlo simulation also shows that droplets are randomly dispersed according to the uniformly random distribution. Comparison with the regular distribution also demontrates that this distribution, although currently used in deriving some models, is not appropriate. Such a result could be useful to specify a characteristic length scale related to the interdroplet distance and more representative of the spray distribution. Ongoing work is done to use the available nonreacting data, further assess these initial results, and extend the experimental database. The six DNS/DPS simulations consider monodisperse solid particles in an isotropic homogeneous turbulence field with six different particle Stokes numbers St. Depending on its value, the particles may or may not experiment preferential concentration effects. Spray analysis can exhibit a dependency between the spray distribution and the Stokes number due to the preferential concentration phenomenon. It also proves that the preferential segregation effect is not important in the present experimental data, thus confirming that the uniformly random distribution is appropriate to describe the flow under consideration.

ACKNOWLEDGMENTS

The work has been realized thanks to the partial financial support of the Région Midi-Pyrénées. The authors would also like to thank F. Bigot for his invaluable involvement in the manufacturing of the Prométhé-LACOM setup.

REFERENCES

Akamatsu, F., Mizutani, Y., Katsuki, M., Tsushima, S., and Cho, Y.D., Measurement of the Local Group Combustion Number of Droplet Clusters in a Premixed Spray Stream, *26th Symposium on Combustion*, Naples, Italy, 1996.

Annamalai, K. and Ryan, W., Interactive Processes in Gasification and Combustion. Part I: Liquid Drop Arrays and Clouds, *Prog. Energy Combust. Sci.*, vol. **18**, pp. 221–295, 1992.

Bansal, P. and Ardell, A., Average Nearest-Neighbor Distances between Uniformly Distributed Finite Particles, *Metallography*, vol. **5**, pp. 97–111, 1972.

Beck, C.H., Koch, R., and Bauer, H.-J., Investigation of the Effect of Incomplete Droplet Prevaporization on NOx Emissions in LDI Combustion Systems, *J. Eng. Gas Turbines Power*, vol. **130**, pp. 1–8, 2008.

Beck, C.H., Koch, R., and Bauer, H.-J., Identification of Droplet Burning Modes in Lean, Partially Prevaporized Swirl-Stabilized Spray Flames, *32th Symposium on Combustion*, Montreal, Canada, 2009.

Borghi, R. and Champion, M., *Modélisation et Théorie des Flammes*, Ed. Technip, 2000.

Boutsikakis, A., Numerical Simulation and Physical Analysis of the Dispersion of Charged Inertial Particles Transported by Stationary Homogeneous Isotropic Turbulence, PhD, INP, 2020.

Candel, S., Lacas, F., Darabiha, N., and Rolon, J.C., A Voir, *Multiphase Sci. Technol.*, vol. **11**, pp. 1–18, 1999.

Chandrasekhar, S., Stochastic Problems in Physics and Astronomy, *Rev. Modern Phys.*, vol. **15**, pp. 1–89, 1943.

Chiu, H.H., Kim, H.Y., and Croke, E.J., Internal Group Combustion of Liquid Droplets, *19th Symposium on Combustion*, Haifa, Israel, 1982.

Correa, S.M. and Sichel, M., The Group Combustion of a Spherical Cloud of Monodisperse Fuel Droplets, *19th Symposium on Combustion*, Haifa, Israel, 1982.

Crowe, C.T., Schwarzkopf, J.D., Sommerfeld, M., and Tsuji, Y., *Multiphase Flows with Droplets and Particles*, Boca Raton, FL: CRC Press, 2011.

Elperin, T. and Krasovitov, B., Analysis of Evaporation and Combustion of Random Clusters of Droplets by a Modified Method of Expansion into Irreducible Multipoles, *Atomization Sprays*, vol. **4**, pp. 79–97, 1994.

Fede, P., Simonin, O., and Villedieu, P., Monte-Carlo Simulation of Colliding Particles or Coalescing Droplets Transported by a Turbulent Flow in the Framework of a Joint Fluid-Particle PDF Approach, *Int. J. Multiphase Flow*, vol. **74**, pp. 165–183, 2015.

Godsave, G., Studies of the Combustion of Drops in a Fuel Spray—The Burning of Single Drops of Fuel, *4th Symposium on Combustion*, University Park, PA, 1953.

Hwang, S.M., Akamatsu, F., and Park, H.-S., Evaluation of Combustion Mechanism of Droplet Cluster by Simultaneous Time-Series Measurement in Premixed Spray Flame, *J. Ind. Eng. Chem.*, vol. **13**, pp. 206–213, 2007.

Imaoka, R. and Sirignano, W., Transient Vaporization and Burning in Dense Droplet Arrays, *Int. J. Heat Mass Transf.*, vol. **58**, pp. 4354–4366, 2005a.

Imaoka, R. and Sirignano, W., Vaporization and Combustion and Burning in Dense Droplet Arrays, *Proc. Combust. Inst.*, vol. **30**, pp. 1981–1989, 2005b.

Jiang, J. and Chiu, H., Multistate Behavior of a Droplet in Dilute Sprays, *Atomization Sprays*, vol. **7**, pp. 479–506, 1997.

Jiang, J. and Chiu, H., Advanced Modelling of Spray Combustion Processes in Airbreathing Propulsion Combustors, *38th AIAA/ASME Propulsion Conf. and Exhibit*, Indianapolis, Indiana, 2002.

Jiang, T. and Chiu, H., Advanced Modelling of Spray Combustion Processes in Airbreathing Propulsion Combustors, *25th Aerospace Sciences Meeting*, Reno, NV, 1987.

Kerstein, A.R. and Law, C.K., Percolation in Combusting Sprays I: Transition from Cluster Combustion to Percolate Combustion in Non-Premixed Sprays, *19th Symposium on Combustion*, Haifa, Israel, 1982.

Kostinski, A. and Jameson, A., On the Spatial Distribution of Cloud Particles, *J. Atmosph. Sci.*, vol. **57**, pp. 901–915, 2000.

Kostinski, A. and Shaw, R., Scale-Dependent Droplet Clustering in Turbulent Clouds, *J. Fluid Mech.*, vol. **434**, pp. 389–398, 2001.

Law, C., Asymptotic Theory for Ignition and Extinction of Droplet Burning, *Combust. Flame*, vol. **24**, pp. 89–98, 1975.

Law, C. and Chung, S., An Ignition Criterion for Droplets in Sprays, *Combust. Sci. Technol.*, vol. **22**, pp. 17–26, 1980.

Lovett, J., Ahmed, K., Bibik, O., Smith, A., Lubarrsky, E., Menon, S., and Zinn, B., On the Influence of Fuel Distribution on the Flame Structure of Bluff-Body Stabilized Flames, *J. Eng. Gas Turbines Power Transact. ASME*, vol. **136**, 2014.

Mawid, M. and Aggarwal, S., Chemical Kinetics Effects on the Ignition of a Fuel Droplet, *Combust. Sci. Technol.*, vol. **65**, pp. 137–150, 1989.

McDonell, V.G., Adachi, M., and Samuelsen, G.S., Structure of Reacting and Non-Reacting Swirling Air-Assisted Sprays, *Combust. Sci. Technol.*, vol. **82**, pp. 225–248, 1992.

Monchaux, R., Bourgoin, M., and Cartelier, A., Analyzing Preferential Concentration and Clustering of Inertial Particles in Turbulence, *Int. J. Multiphase Flow*, vol. **40**, pp. 1–18, 2012.

Neumann, P. and Umbauer, H., Characterization of the Spatial Distribution State of Particles Transported by a Turbulent Gas Flow, *Exp. Fluids*, vol. **12**, pp. 81–89, 1991.

Paulhiac, D., Modélisation de la Combustion d'un Spray dans un Brûleur Aéronautique, PhD, Université de Toulouse, 2015.

Paulhiac, D., Cuenot, B., Riber, E., Esclapez, L., and Richard, S., Analysis of the Spray Flame Structure in a Lab-Scale Burner Using Large Eddy Simulations and Discrete Particle Simulation, *Combust. Flame*, vol. **212**, pp. 25–38, 2020.

Reveillon, J. and Vervisch, L., Analysis of Weakly Turbulent Dilute-Spray Flames and Spray Combustion Regimes, *J. Fluid Mech.*, vol. **537**, pp. 317–347, 2005.

Rouzaud, O., Vicentini, M., Lecourt, R., Simonin, O., and Bodoc, V., Experimental Analysis of Droplet Spatial Distribution in a Spray Burner, *Proceeding of the ILASS Conf.*, Brighton, UK, 2016.

Sahu, S., Hardalupas, Y., and Taylor, A., Droplet-Turbulence Interaction in a Confined Polydispersed Spray: Effect of Droplet Size and Flow Length Scales on Spatial Droplet-Gas Velocity Correlations, *J. Fluid Mech.*, vol. **741**, pp. 98–138, 2014.

Sahu, S., Hardalupas, Y., and Taylor, A., Droplet-Turbulence Interaction in a Confined Polydispersed Spray: Effect of Turbulence on Droplet Dispersion, *J. Fluid Mech.*, vol. **794**, pp. 267–309, 2016.

Sahu, S., Hardalupas, Y., and Taylor, A., Interaction of Droplet Dispersion and Evaporation in a Polydispersed Spray, *J. Fluid Mech.*, vol. **846**, pp. 37–81, 2018.

Simonin, O., Zaichik, L., Alipchenkov, V., and Février, P., Connection between Two Statistical Approaches for the Modelling of Particle Velocity and Concentration Distributions in Turbulent Flow: The Mesoscopic Eulerian Formalism and the Two-Point Probability Density Function Method, *Phys. Fluids*, vol. **18**, 2006.

Spalding, D., The Combustion of Liquid Fuels, *4th Symposium on Combustion*, University Park, PA, 1953.

Squires, K. and Eaton, J., Preferential Concentration of Particles by Turbulence, *Phys. Fluids*, vol. **3**, 1991.

Vicentini, M., Mise en Évidence Expérimentale et Modélisation des Régimes de Combustion Diphasique Présents dans les Foyers Aéronautiques, PhD, Université de Toulouse, 2016.

Vicentini, M., Lecourt, R., Bodoc, V., Rouzaud, O., and Simonin, O., Régimes de Combustion dans les Foyers Aéronautiques: Mise en Place Expérimentale de l'Écoulement Diphasique, *14ème Congrès Francophone de Techniques Laser*, CFTL Proceedings, 2014.

Vicentini, M., Lecourt, R., Bodoc, V., Rouzaud, O., and Simonin, O., Experimental Investigation of Spray Combustion Regimes in Aero-Engines Combustors, *6th European Conf. for Aeronautics and Space Sciences*, Kraków, Poland, 2015.

Virepinte, J.-F., Adam, O., Biscos, Y., and Lavergne, G., Droplet Spacing on Drag Measurement and Burning Rate for Isothermal and Reacting Conditions, *J. Propuls.*, vol. **15**, pp. 97–102, 1999.

Wang, F., Hu, B., and Huang, Y., A Two-Phase Turbulent Combustion Model and Its Validation for Spray Flames, *Fuel*, vol. **113**, pp. 280–286, 2013.

APPENDIX A.

Consider a two-dimensional spray with a mean droplet number density $\bar{n}$ and assume that its spatial distribution is randomly uniform. It obeys the Poisson law:

$$\mathcal{P}(\lambda, k) = \frac{\lambda^k}{k!}\exp(-\lambda)$$

where the parameter k corresponds to the number of droplets enclosed in a surface and λ is the product of the mean density and the surface. Considering a droplet, the probability $\mathcal{H}(D_i)$ that its nearest neighbor is located at a distance D_i is equivalent to the product of the probability of having no droplet enclosed in the surface πD_i^2 times the probability of having a droplet between D_i and $D_i + dD_i$. Thus we have

$$\mathcal{H}(D_i) = 2\pi\bar{n}D_i \exp\left(-\pi\bar{n}D_i^2\right)$$

By definition, the mean value of the nearest neighbor is

$$\mathsf{E}(D_i) = \int_o^\infty D_i 2\pi\bar{n}D_i \exp\left(-\pi\bar{n}D_i^2\right) dD_i$$

Using the intermediate variable $u = \pi\bar{n}D_i^2$ and after some algebraic operations, the mean value expression is

$$\mathsf{E}(D_i) = \frac{1}{\sqrt{\pi}}\bar{n}^{-1/2}\,\Gamma\left(\frac{3}{2}\right)$$

By definition, the variance of this variable is

$$\mathsf{Var}(D_i) = \int_o^\infty \left[D_i - \mathsf{E}(D_i)\right]^2 2\pi\bar{n}D_i \exp\left(-\pi\bar{n}D_i^2\right) dD_i = \frac{1}{\pi\bar{n}}\left[\Gamma(2) - \Gamma\left(\frac{3}{2}\right)^2 \Gamma(1)\right]$$

or, equivalently, using the standard deviation,

$$\sigma(D_i) = \frac{1}{\sqrt{\pi\bar{n}}}\left[\Gamma(2) - \Gamma\left(\frac{3}{2}\right)^2 \Gamma(1)\right]^{1/2}$$

These formulas use different values of the Gamma function: $\Gamma(1) = 1$, $\Gamma(3/2) = \sqrt{\pi}/2$, $\Gamma(2) = 1$. By replacing these values inside the relationships, we finally obtain Eq. (14).

For the three-dimensional case, refer to Chandrasekhar (1943).